Estimates of North African methane emissions from 2010-2017 using GOSAT observations

Luke M. Western,*,† Alice E. Ramsden,‡ Anita L. Ganesan,‡ Hartmut Boesch,¶,§ Robert J. Parker,¶,§ Tia R. Scarpelli,‖ Rachel L. Tunnicliffe,† and Matthew Rigby†

†*School of Chemistry, University of Bristol, Bristol, BS8 1TS, UK*

‡*School of Geographical Sciences, University of Bristol, Bristol, BS8 1SS, UK*

¶*National Centre for Earth Observation, University of Leicester, Leicester, LE1 7RH, UK*

§*Earth Observation Science, School of Physics and Astronomy, University of Leicester, Leicester, LE1 7RH, UK*

‖*Earth and Planetary Sciences, Harvard University, Cambridge, 02138, USA*

E-mail: luke.western@bristol.ac.uk

Abstract

Source characteristics of methane emissions in Africa are not well understood, despite methane's role as the second largest anthropogenic contributor to climate change. Here, we present monthly methane emission estimates from Algeria, Egypt, Libya, Morocco and Tunisia between 2010-2017, a region dominated by anthropogenic emissions. Emissions are estimated using observations from the GOSAT satellite and a Markov chain Monte Carlo inverse algorithm. Our top-down North African methane emissions are generally in line with inventory estimates and national reporting to the United Nations Framework Convention on Climate Change (UNFCCC). An exception is that summertime emissions from the Nile Delta region are considerably higher those that

predicted by inventory estimates, possibly due to agricultural practices and the influence of the Nile.

Introduction

Global atmospheric concentrations methane have been rising since a hiatus was observed between the early 2000s and 2007[1]. The reason for this pause and renewed growth is poorly understood; previous studies have implicated the main drivers of change to be an increase in anthropogenic emissions[2,3], natural sources[4], reduced biomass burning and rising fossil fuel emissions[3] or a potential change in the main sink of methane, the global concentrations of atmospheric OH radicals[5,6].

With very few ground-based measurements of methane on the African continent, there is uncertainty about the potential role that African methane sources have played in recent growth. There is evidence that methane emissions from tropical Africa could explain around a third of a global emissions increase, primarily due to a rise in emissions from the Sudd in South Sudan[7,8]. This paper presents estimates of methane emissions between 2010-2017 from North Africa, here defined as Algeria, Egypt, Libya, Morocco (including Western Sahara) and Tunisia.

In this region, fugitive emissions from oil and natural gas production dominate and account for around half of the total bottom-up estimated emissions[9]. Between 2010-2017 North Africa produced between 2.3 - 4.3 % of global petroleum and ~5 % of natural gas[10]. See the supporting information for a further breakdown of North Africa's fossil fuel production.

As non-Annex I countries under the United Nations Framework Convention on Climate Change (UNFCCC), these nations are not required to submit annual greenhouse gas reports. However, all countries, except Libya, have submitted anthropogenic emissions estimates through National Communications to the UNFCCC, although these emission estimates may have high uncertainties. Algeria has estimated its methane emissions for 2000 (i.e. before this period of study) as 1.58 Tg[11]; Egypt has estimated its 2015 emissions as 1.98 Tg[12]; Morocco as 0.51 Tg in 2010, 0.54 Tg in 2012, 0.55 Tg in 2014 and 0.59 Tg in 2016[13]; and Tunisia as 0.28 Tg in 2010 and 0.29 Tg in 2012[14].

Given the paucity of ground-based methane measurements in North Africa, we have used observations of column-average methane concentrations from the GOSAT satellite, combined with the atmospheric transport model NAME (Numerical Atmospheric dispersion Modelling Environment)[15] to infer methane emissions. Below, we outline the emissions inference framework, present our result for each country, and discuss implications for the methane budget of this region.

Materials and Methods

GOSAT Observations

We use observations of dry air column-average methane concentrations to inferencer methane emissions in North Africa. These measurements are made from the Thermal And Near-infrared Sensor for carbon Observation Fourier Transform Spectrometer (TANSO-FTS) on board the GOSAT satellite[16]. The product comes from the University of Leicester GOSAT-OPCR v7.2 proxy dry air column-average methane retrieval[17,18], $XCH_{4\,proxy}$. The $XCH_{4\,proxy}$ retrieval uses total column values of methane (XCH_4) and carbon dioxide (XCO_2) using spectral windows at 1.65 and 1.61 μm for XCH_4 and XCO_2 respectively. The ratio of XCH_4 to XCO_2 is multiplied by an model ensemble-derived estimate of column-average carbon dioxide mole fraction to estimate $XCH_{4\,proxy}$. This method produces robust retrievals in the presence of clouds and aerosols due to their common influence on XCH_4 and XCO_2, however may be subject to larger uncertainties in regions where CO_2 measurements are not prevalent. We limit the XCH_4 observations to the spatial extent of -15° W to 38° E and 15° N to 34 ° N and bin the observations to the resolution of the output of the atmospheric transport model used in the inversion (NAME transport model section,0.352° by 0.234°). Between April 2010 and the end of 2017, there is a mean of 1119 observations per month, with little seasonality in observation coverage over this region (see Figure S4). Figure S5 shows the binned average GOSAT $XCH_{4\,proxy}$ observations for November 2011 - April 2012 and May 2012 - October 2012.

NAME transport model

We use the approach outlined in Ganesan et al.[19] and Tunnicliffe et al.[20] to relate XCH_4 observations to surface emissions. The sensitivity of the $XCH_{4\,proxy}$ measurements to surface emissions are derived using the Lagrangian particle dispersion model NAME[15] run in backward mode. The sensitivities derived from the NAME model output have a resolution of 0.352° by 0.234° and we employ a simulation domain of -50 to 87 °E by -15 to 41 °N degrees (Figure S6) to a height of 20 km.

Meteorological fields from the Met Office Unified Model model[21] drive transport within NAME, and have a temporal resolution of three hours and a spatial resolution that increases throughout the study period from 0.352 by 0.234° in 2010 to 0.141 by 0.094° in 2017. We run NAME for each of the 20 vertical levels defined within the $XCH_{4\,proxy}$ product. Particles are released from each level and the interaction with the surface (below 40 magl) and boundaries are recorded[20]. We combine the sensitivities from the vertical layers into a single sensitivity of the $XCH_{4\,proxy}$ observation to emissions by weighting each level according to the corresponding GOSAT averaging kernel and pressure weight from the retrieval[19,22]. The boundary sensitivities are combined into four scaling parameters each month in the inversion, which uniformly scales the a priori boundary condition curtains on each horizontal boundary.

We assume that the modelling error is stochastic with an uncertain standard deviation, where the standard deviation is given a prior 95% uncertainty of 5.5-14.7 ppb.

A priori methane emissions

We base our a priori estimates of methane emissions on various sources, regridded to that of the output of the transport model (NAME transport model section). Fugitive emissions from oil, coal and gas, the dominant a priori emissions source in North Africa, are from Scarpelli et al.[9] and are a static annual climatology. The GFED v4.1 database[23] provides the emissions for natural and anthropogenic biomass burning. Emissions from wetlands come from the mean of the ensembles of the WetCHARTs database[24], where values for 2015 are repeated for 2016 and 2017. Any emissions from rice paddies come from a monthly inventory for the year 2000[25]. Other anthropogenic emissions, such as enteric fermentation, landfills, road transport, shipping and manufacturing, come from the EDGAR v.4.3.2 emissions inventory by sector for 2012[26]. We assume all other emissions (e.g. termites and geological sources) to be negligible. Inventory estimates for Morocco are generally in line with emissions reported to the UNFCCC. Egypt's 2015 reporting is around 50% higher than the a priori emissions, and Tunisia's reporting is around 30-35% higher.

The a priori emissions for the region are 5.0 Tg year^{-1} between 2010 - 2017 (5.1 Tg year^{-1} in 2015). We treat these emissions as very uncertain, and assign a 95% uncertainty range for the a priori emissions of 2.7-12.8 Tg year^{-1} in 2010 to 2.7-13.0 Tg year^{-1} in 2017, following a log-normal distribution, where the mode of the distribution is the a priori emissions. This distribution has been chosen as it approximately follows the geometric standard deviation uncertainty (for a lognormal 68 % uncertainty) for Annex I countries in Scarpelli et al.[9], the dominant emissions source.

Boundary conditions

As we infer emissions in a limited domain, the sensitivity of the methane concentrations to contributions from the domain edges must be quantified. The a priori boundary condition mole fraction curtains at the domain edges come from the ECMWF CAMS reanalysis database (which has not been constrained using GOSAT data)[27]. We take the a priori estimate each month to be the mean state at the NAME domain edges. The derived emissions are mostly insensitive to the choice of a priori mole fraction at the boundary (see the supporting information).

Inverse Method

Here we represent the problem of emissions and boundary condition inference as a statistical model. We denote the $\mathrm{XCH}_4^{\mathrm{proxy}}$ observations (see section GOSAT Observations) as the vector, $\mathbf{y}$, which can be modelled by the linear forward model

$$\mathbf{y} = \mathbf{H}\mathbf{x} + \mathbf{K}\mathbf{u} + \epsilon, \tag{1}$$

where $\mathbf{H}$ is the sensitivity matrix to emissions at the surface and $\mathbf{K}$ is the sensitivity to the boundaries, produced using NAME (section NAME transport model) with each row multiplied by the a priori estimates from sections and for $\mathbf{H}$ and $\mathbf{K}$ respectively, $\mathbf{x}$ contains a vector which scales the a priori emissions by some factor, $\mathbf{u}$ is as $\mathbf{x}$ for the boundary conditions, and ϵ is the stochastic model-measurement error. We assume that all observations in $\mathbf{y}$ are independent and identically distributed with a known stochastic measurement error σ_{obs} and unknown model error σ_{mod}, which combine as $\sigma_y = \sqrt{\sigma_{\mathrm{obs}}^2 + \sigma_{\mathrm{mod}}^2}$ (in ppb), where the resulting covariance matrix is $\mathbf{R} = \mathbf{I}\sigma_y^2$, and $\mathbf{I}$ is the identity matrix. We follow a typical Bayesian framework,

$$\mathrm{p}(\mathbf{x}, \mathbf{u}, \sigma_{\mathrm{mod}} \mid \mathbf{y}) \propto \mathrm{p}(\mathbf{y} \mid \mathbf{x}, \mathbf{u}, \sigma_{\mathrm{mod}})\, \mathrm{p}(\mathbf{x}, \mathbf{u}, \sigma_{\mathrm{mod}}). \tag{2}$$

Our hierarchical model is then

$$\mathbf{y} \mid \mathbf{x}, \mathbf{u}, \sigma_{\text{mod}} \overset{\text{iid}}{\sim} \mathcal{N}(\mathbf{Hx} + \mathbf{Ku}, \mathbf{R}), \tag{3}$$

$$\mathbf{x} \overset{\text{iid}}{\sim} \mathcal{LN}(0.16, 0.4^2), \tag{4}$$

$$\mathbf{u} \overset{\text{iid}}{\sim} \mathcal{LN}(0.004, 0.02^2), \tag{5}$$

$$\sigma_{\text{mod}} \sim \mathcal{LN}(2.2, 0.25^2), \tag{6}$$

where $\mathcal{N}(\cdot)$ and $\mathcal{LN}(\cdot)$ refer to the Normal and Lognormal distributions respectively.

We infer the emissions and influence from the boundary conditions using hierarchical Bayesian inference[28]. Sampling uses a two-stage sampler as in Say et al.[29]. Firstly, a No-U-Turn (NUTS) sampler[30] samples the latent field $\mathbf{x}$. A NUTS sampler is an extension to Hamiltonian Monte Carlo, which has previously been used for inference of trace-gas emissions[31,32]. A slice sampler[33], which computationally faster per iteration, samples the hyperparameter σ_{mod} as a second step in the sampling process.

We infer methane emissions for each calendar month between April 2010 through 2017, and assume that methane emissions are constant over each period of inference.

The elements of the latent field containing emissions are a basis function representation of the NAME domain. We follow the approach of Say et al.[29], and optimise 100 basis functions based on the a priori above-background mole fraction contribution in space using a quadtree algorithm[34]. The algorithm recursively divides the basis function into four new basis functions until the desired number of basis functions is achieved, giving a higher spatial resolution where there is a greater above-background a priori mole fraction contribution and lower elsewhere (see Fig. S6).

We run the NUTS-slice sampler over a total of 250,000 iterations (burning the first 50,000), with multiple chains running in parallel. To check for convergence we use a Gelman-Rubin diagnostic[35], ensuring all chains reach a criteria less than 1.05. The uncertainty in the inferred emissions are quantified using the Highest Posterior Density (HPD) region (see

Box and Tiao[36] and supporting information).

Under this statistical model it is possible to infer the latent variables, namely the emissions of methane and the boundary conditions, and the hyperparameter controlling the uncertainty in the model error.

Results and Discussion

For Morocco, Algeria, Tunisia and Libya, the a priori estimates and UNFCCC National Communications fall within the posterior 95% uncertainty, or are slightly underestimated, for periods where reports are available. This would suggest that the inventories detailed in the A priori methane emissions section, and the emissions estimates in UNFCCC National Communications are largely consistent for these countries. Figure 1 shows the posterior estimated emissions over the study period, where all emissions in the region were constrained by the inversion (Figure S7). Figure S8 and Table S1 present these emissions as annual means.

Estimated emissions from Egypt are consistently larger than the a priori estimates, although they are smaller in 2015 than those reported in their National Communication. The most noticeable discrepancy to the a priori estimate (Figure 1) is that Egypt has large, unexpected methane emission during the summer months, lasting from around June to October. These summer emissions are uncorrelated with aerosol optical depth measurements in the region[37]. An increase in emissions for these months is observed in the a priori estimates, attributed to rice cultivation[25], although to a much lesser extent than in the posterior estimates. These unexpected emissions come from north of Egypt, in the region containing the Nile Delta, starting approximately north of the Aswan High Dam. Figure 3a shows the the posterior mean flux estimate, and Figure 3b shows the a priori flux, as an average for August over all years. These emissions in Egypt coincide with the summer agricultural growing season, with high temperatures and high levels of irrigation. This is in contrast to the rest of North Africa, where the main growing season is during the winter months, and primarily driven by rainfall (see the supporting information for more discussion on agricultural methane emissions outside of Egypt). Irrigation of crops in Egypt is generally fed by branching canals, and drainage ditches[38], necessary due to the low levels of rainfall in the region. As a result, high levels of irrigation are needed during the summer, with rice and summer maize requiring the highest gross irrigation in the region[39] and sugarcane requiring the highest levels of irrigation per square metre, followed by rice[40]. Our a priori annual mean estimate for agriculture (including rice) in Egypt using bottom up inventories is 0.40 Tg, which is much smaller than 0.77 Tg in Egypt's 2015 UNFCCC reporting. Figure 2 shows the mean posterior estimated emissions for each month, alongside the daily mean temperature at Cairo for each month, and the monthly satellite-estimated discharge from Lake Nasser (feeding the Nile after the Aswan High Dam) from 2005-2008[41]. Although the satellite-derived estimated discharge is not a direct indicator of water used for irrigation, it is an indicator of the inflow to the Nile Delta. Figure 2 shows that the maximum in emissions coincides within ± 1 month, with the maximum temperature or discharge. An exception is that there is little to no summertime emissions increase in 2015, when North Africa experienced a drought[42]. Water levels of Lake Nasser[43] generally sharply drop in summertime, coincident with larger discharge (Figure S9). Figure S9 shows that 2015 water levels had no such drop and rise, perhaps indicating changes to discharge into the Nile Delta in 2015. This is likely due to the droughts caused by the strong El Niño event in 2015, which impacted the Nile river flow[44–46] and global methane emissions[47]. It is therefore likely that current agricultural flooding practices, combined with high temperatures, are a major driver in the Nile Delta's methane emissions. These findings corroborate evidence of the influence of the (White) Nile on Africa's methane emissions[7].

The biogeochemistry of methane release from fresh water is difficult to generalise, although an increase in the area of water bodies within Egypt, coupled with warmer temperatures, would likely lead to increased methane emissions[48–51]. Previous studies show that river outflows from dammed reservoirs can release considerable levels of methane[52], although these processes have generally been observed at distances far closer to the dam itself than from the Aswan High Dam to the bulk of emissions in the Nile Delta[53,54].

For validation of our results, we use weekly flask-air measurements from the Italian island of Lampedusa[55,56] (12.62°E, 35.52°N), which provides continuous measurements throughout our period of study. Measured and forward modelled observations agree qualitatively (Fig. S3), although the low-frequency of the measurements, which are primarily representative of background air, make a more rigorous inter-comparison challenging.

Methane emissions from North Africa do not appear to have changed significantly (overall trend of -0.2 ± 0.6 Tg year^{-1}, 95% uncertainty). However, our finding of a substantial and unexpected seasonal source in the Nile Delta suggests that that agricultural emissions from the region have been under-estimated in our a priori estimate. This may indicate a wider issue of under-quantified emissions from agronomically managed temporary wetland ecosystems.

Ever increasing volumes of earth observation data at higher spatial resolution will allow further regional scale studies to monitor changes in methane emission trends.

Code and data availability

ECMWF CAMS reanalysis data were downloaded from the Copernicus Atmosphere Monitoring Service (CAMS) Atmosphere Data Store (ADS) `https://ads.atmosphere.copernicus.eu/cdsapp#!/dataset/cams-global-reanalysis-eac4?tab=overview`. Lake products courtesy of the USDA/NASA G-REALM program at `https://ipad.fas.usda.gov/cropexplorer/global_reservoir/`. The latest version of the University of Leicester GOSAT Proxy v9.0 XCH_4 data are available from the Centre for Environmental Data Analysis data repository at `https://doi.org/10.5285/18ef8247f52a4cb6a14013f8235cc1eb` (Parker and Boesch, 2020). The version used in this study (v7.2) is available from the Copernicus C3S Climate Data Store at `https://cds.climate.copernicus.eu`. Flask-air measurements from

Lampedusa are available at `ftp://aftp.cmdl.noaa.gov/data/trace_gases/ch4/flask/surface/`. The inversion results from this work, including all inputs to the inverse model, is available at `https://osf.io/cdae3/` (Western 2021; DOI 10.17605/OSF.IO/CDAE3). Access to the inversion code is available on request from the corresponding author.

Acknowledgement

We thank Eric Muala for supplying satellite estimated discharge data for Lake Nasser. We thank the Japanese Aerospace Exploration Agency, National Institute for Environmental Studies and the Ministry of Environment for the GOSAT data and their continuous support as part of the Joint Research Agreement. This research used the ALICE High Performance Computing Facility at the University of Leicester for the GOSAT retrievals. LMW, RT and MR were supported by Natural Environment Research Council (NERC) grants NE/N016548/1, NE/S016155/1, ALG was supported by a NERC Independent Research Fellowship, NE/L010992/1, and AR was supported by a studentship from the NERC GW4+ Doctoral Training Partnership. Robert J. Parker and Hartmut Boesch are funded via the UK National Centre for Earth Observation (NE/R016518/1 and NE/N018079/1).

Supporting information

The supporting information consists of sections describing North African petroleum and natural gas production; a description and presentation of the derived emissions using different a priori boundary conditions; a description of the highest posterior density region; a discussion on agricultural emissions outside of Egypt; validation of the results against measurements made at Lampedusa in Italy and the supplementary tables and figures referred to in the main text.

References

(1) Rigby, M.; Prinn, R. G.; Fraser, P. J.; Simmonds, P. G.; Langenfelds, R. L.; Huang, J.; Cunnold, D. M.; Steele, L. P.; Krummel, P. B.; Weiss, R. F.; O'Doherty, S.; Salameh, P. K.; Wang, H. J.; Harth, C. M.; Mühle, J.; Porter, L. W. Renewed growth of atmospheric methane. *Geophysical Research Letters* **2008**, *35*.

(2) Schaefer, H.; Fletcher, S. E. M.; Veidt, C.; Lassey, K. R.; Brailsford, G. W.; Bromley, T. M.; Dlugokencky, E. J.; Michel, S. E.; Miller, J. B.; Levin, I.; Lowe, D. C.; Martin, R. J.; Vaughn, B. H.; White, J. W. C. A 21st-century shift from fossil-fuel to biogenic methane emissions indicated by $^{13}CH_4$. *Science* **2016**, *352*, 80–84.

(3) Worden, J. R.; Bloom, A. A.; Pandey, S.; Jiang, Z.; Worden, H. M.; Walker, T. W.; Houweling, S.; Röckmann, T. Reduced biomass burning emissions reconcile conflicting estimates of the post-2006 atmospheric methane budget. *Nature Communications* **2017**, *8*.

(4) Nisbet, E. G.; Dlugokencky, E. J.; Manning, M. R.; Lowry, D.; Fisher, R. E.; France, J. L.; Michel, S. E.; Miller, J. B.; White, J. W. C.; Vaughn, B.; Bousquet, P.; Pyle, J. A.; Warwick, N. J.; Cain, M.; Brownlow, R.; Zazzeri, G.; Lanoisellé, M.; Manning, A. C.; Gloor, E.; Worthy, D. E. J. et al. Rising atmospheric methane: 2007-2014 growth and isotopic shift. *Global Biogeochemical Cycles* **2016**, *30*, 1356–1370.

(5) Rigby, M.; Montzka, S. A.; Prinn, R. G.; White, J. W. C.; Young, D.; O'Doherty, S.; Lunt, M. F.; Ganesan, A. L.; Manning, A. J.; Simmonds, P. G.; Salameh, P. K.; Harth, C. M.; Mühle, J.; Weiss, R. F.; Fraser, P. J.; Steele, L. P.; Krummel, P. B.; McCulloch, A.; Park, S. Role of atmospheric oxidation in recent methane growth. *Proceedings of the National Academy of Sciences* **2017**, *114*, 5373–5377.

(6) Turner, A. J.; Frankenberg, C.; Wennberg, P. O.; Jacob, D. J. Ambiguity in the causes

for decadal trends in atmospheric methane and hydroxyl. *Proceedings of the National Academy of Sciences* **2017**, *114*, 5367–5372.

(7) Lunt, M. F.; Palmer, P. I.; Feng, L.; Taylor, C. M.; Boesch, H.; Parker, R. J. An increase in methane emissions from tropical Africa between 2010 and 2016 inferred from satellite data. *Atmospheric Chemistry and Physics* **2019**, *19*, 14721–14740.

(8) Pandey, S.; Houweling, S.; Lorente, A.; Borsdorff, T.; Tsivlidou, M.; Bloom, A. A.; Poulter, B.; Zhang, Z.; Aben, I. Using satellite data to identify the methane emission controls of South Sudan's wetlands. *Biogeosciences* **2021**, *18*, 557–572.

(9) Scarpelli, T. R.; Jacob, D. J.; Maasakkers, J. D.; Sulprizio, M. P.; Sheng, J.-X.; Rose, K.; Romeo, L.; Worden, J. R.; Janssens-Maenhout, G. A global gridded ($0.1° \times 0.1°$) inventory of methane emissions from oil, gas, and coal exploitation based on national reports to the United Nations Framework Convention on Climate Change. *Earth System Science Data* **2020**, *12*, 563–575.

(10) EIA, EIA: International Energy Statistics. http://eia.gov/beta/international/ (accessed 22 January 2021).

(11) Ministere de l'Amenagement du Territoire et de l'Environnement, Seconde Communication Nationale de l'Algerie sur les Changements Climatiques a la CCNUCC. 2010.

(12) Ministry of Environment: Egyptian Environmental Affairs Agency, Egypt's First Biennial Update Report to the United Nations Framework Convention on Climate Change. 2018.

(13) Départment de l'Environment, Deuxième Rapport Biennal actualisé du Maroc dans le cadre de la CCNUCC. 2019.

(14) Ministère des Affaires Locales et de l'Environnement, Deuxième Rapport Biennal de la Tunisie. 2016.

(15) Jones, A.; Thomson, D.; Hort, M.; Devenish, B. The U.K. Met Office's Next-Generation Atmospheric Dispersion Model, NAME III. *Air Pollution Modeling and Its Application XVII* **2006**, 580–589.

(16) Kuze, A.; Suto, H.; Nakajima, M.; Hamazaki, T. Thermal and near infrared sensor for carbon observation Fourier-transform spectrometer on the Greenhouse Gases Observing Satellite for greenhouse gases monitoring. *Applied Optics* **2009**, *48*, 6716.

(17) Parker, R.; Boesch, H.; Cogan, A.; Fraser, A.; Feng, L.; Palmer, P. I.; Messerschmidt, J.; Deutscher, N.; Griffith, D. W. T.; Notholt, J.; Wennberg, P. O.; Wunch, D. Methane observations from the Greenhouse Gases Observing SATellite: Comparison to ground-based TCCON data and model calculations. *Geophysical Research Letters* **2011**, *38*.

(18) Parker, R. J.; Webb, A.; Boesch, H.; Somkuti, P.; Barrio Guillo, R.; Di Noia, A.; Kalaitzi, N.; Anand, J. S.; Bergamaschi, P.; Chevallier, F.; Palmer, P. I.; Feng, L.; Deutscher, N. M.; Feist, D. G.; Griffith, D. W. T.; Hase, F.; Kivi, R.; Morino, I.; Notholt, J.; Oh, Y.-S. et al. A decade of GOSAT Proxy satellite CH_4 observations. *Earth System Science Data* **2020**, *12*, 3383–3412.

(19) Ganesan, A. L.; Rigby, M.; Lunt, M. F.; Parker, R. J.; Boesch, H.; Goulding, N.; Umezawa, T.; Zahn, A.; Chatterjee, A.; Prinn, R. G.; Tiwari, Y. K.; van der Schoot, M.; Krummel, P. B. Atmospheric observations show accurate reporting and little growth in India's methane emissions. *Nature Communications* **2017**, *8*.

(20) Tunnicliffe, R. L.; Ganesan, A. L.; Parker, R. J.; Boesch, H.; Gedney, N.; Poulter, B.; Zhang, Z.; Lavrič, J. V.; Walter, D.; Rigby, M.; Henne, S.; Young, D.; O'Doherty, S. Quantifying sources of Brazil's CH_4 emissions between 2010 and 2018 from satellite data. *Atmospheric Chemistry and Physics* **2020**, *20*, 13041–13067.

(21) Walters, D. N.; Williams, K. D.; Boutle, I. A.; Bushell, A. C.; Edwards, J. M.; Field, P. R.; Lock, A. P.; Morcrette, C. J.; Stratton, R. A.; Wilkinson, J. M.; Wil-

lett, M. R.; Bellouin, N.; Bodas-Salcedo, A.; Brooks, M. E.; Copsey, D.; Earnshaw, P. D.; Hardiman, S. C.; Harris, C. M.; Levine, R. C.; MacLachlan, C. et al. The Met Office Unified Model Global Atmosphere 4.0 and JULES Global Land 4.0 configurations. *Geoscientific Model Development* **2014**, *7*, 361–386.

(22) O'Dell, C. W.; Connor, B.; Bösch, H.; O'Brien, D.; Frankenberg, C.; Castano, R.; Christi, M.; Eldering, D.; Fisher, B.; Gunson, M.; McDuffie, J.; Miller, C. E.; Natraj, V.; Oyafuso, F.; Polonsky, I.; Smyth, M.; Taylor, T.; Toon, G. C.; Wennberg, P. O.; Wunch, D. The ACOS CO_2 retrieval algorithm: Part 1: Description and validation against synthetic observations. *Atmospheric Measurement Techniques* **2012**, *5*, 99–121.

(23) van der Werf, G. R.; Randerson, J. T.; Giglio, L.; van Leeuwen, T. T.; Chen, Y.; Rogers, B. M.; Mu, M.; van Marle, M. J. E.; Morton, D. C.; Collatz, G. J.; Yokelson, R. J.; Kasibhatla, P. S. Global fire emissions estimates during 1997-2016. *Earth System Science Data* **2017**, *9*, 697–720.

(24) Bloom, A. A.; Bowman, K. W.; Lee, M.; Turner, A. J.; Schroeder, R.; Worden, J. R.; Weidner, R.; McDonald, K. C.; Jacob, D. J. A global wetland methane emissions and uncertainty dataset for atmospheric chemical transport models (WetCHARTs version 1.0). *Geoscientific Model Development* **2017**, *10*, 2141–2156.

(25) Yan, X.; Akiyama, H.; Yagi, K.; Akimoto, H. Global estimations of the inventory and mitigation potential of methane emissions from rice cultivation conducted using the 2006 Intergovernmental Panel on Climate Change Guidelines. *Global Biogeochemical Cycles* **2009**, *23*, n/a–n/a.

(26) Janssens-Maenhout, G.; Crippa, M.; Guizzardi, D.; Muntean, M.; Schaaf, E.; Dentener, F.; Bergamaschi, P.; Pagliari, V. EDGAR v4.3.2 Global Atlas of the three major Greenhouse Gas Emissions for the period 1970-2012. *Open Access* **2017**, 55.

(27) Inness, A.; Ades, M.; AgustÃ-Panareda, A.; BarrÃ©, J.; Benedictow, A.; Blech-

schmidt, A.-M.; Dominguez, J. J.; Engelen, R.; Eskes, H.; Flemming, J.; Huijnen, V.; Jones, L.; Kipling, Z.; Massart, S.; Parrington, M.; Peuch, V.-H.; Razinger, M.; Remy, S.; Schulz, M.; Suttie, M. The CAMS reanalysis of atmospheric composition. *Atmospheric Chemistry and Physics* **2019**, *19*, 3515–3556.

(28) Ganesan, A. L.; Rigby, M.; Zammit-Mangion, A.; Manning, A. J.; Prinn, R. G.; Fraser, P. J.; Harth, C. M.; Kim, K.-R.; Krummel, P. B.; Li, S.; MÃ¼hle, J.; O'Doherty, S. J.; Park, S.; Salameh, P. K.; Steele, L. P.; Weiss, R. F. Characterization of uncertainties in atmospheric trace gas inversions using hierarchical Bayesian methods. *Atmospheric Chemistry and Physics* **2014**, *14*, 3855–3864.

(29) Say, D.; Kuyper, B.; Western, L.; Khan, M. A. H.; Lesch, T.; Labuschagne, C.; Martin, D.; Young, D.; Manning, A. J.; O'Doherty, S.; Rigby, M.; Krummel, P. B.; Davies-Coleman, M. T.; Ganesan, A. L.; Shallcross, D. E. Emissions and Marine Boundary Layer Concentrations of Unregulated Chlorocarbons Measured at Cape Point, South Africa. *Environmental Science & Technology* **2020**, *54*, 10514–10523.

(30) Hoffman, M. D.; Gelman, A. The No-U-Turn Sampler: Adaptively Setting Path Lengths in Hamiltonian Monte Carlo. *Journal of Machine Learning Research* **2014**, *15*, 1593–1623.

(31) Zammit-Mangion, A.; Cressie, N.; Ganesan, A. L.; O'Doherty, S.; Manning, A. J. Spatio-temporal bivariate statistical models for atmospheric trace-gas inversion. *Chemometrics and Intelligent Laboratory Systems* **2015**, *149*, 227–241.

(32) Zammit-Mangion, A.; Cressie, N.; Ganesan, A. L. Non-Gaussian bivariate modelling with application to atmospheric trace-gas inversion. *Spatial Statistics* **2016**, *18*, 194–220.

(33) Neal, R. M. Slice sampling. *The Annals of Statistics* **2003**, *31*, 705–767.

(34) Finkel, R. A.; Bentley, J. L. Quad trees a data structure for retrieval on composite keys. *Acta Informatica* **1974**, *4*, 1–9.

(35) Gelman, A.; Rubin, D. B. Inference from Iterative Simulation Using Multiple Sequences. *Statistical Science* **1992**, *7*, 457–472, Publisher: Institute of Mathematical Statistics.

(36) Box, G. E. P.; Tiao, G. C. *Bayesian inference in statistical analysis*, Wiley Classics Library ed. ed.; A Wiley-Interscience publication; Wiley: New York, 1992; OCLC: 25247039.

(37) El-Metwally, M.; Alfaro, S. C.; Abdel Wahab, M. M.; Zakey, A. S.; Chatenet, B. Seasonal and inter-annual variability of the aerosol content in Cairo (Egypt) as deduced from the comparison of MODIS aerosol retrievals with direct AERONET measurements. *Atmospheric Research* **2010**, *97*, 14–25.

(38) El-Agha, D. E.; Molden, D. J.; Ghanem, A. M. Performance assessment of irrigation water management in old lands of the Nile delta of Egypt. *Irrigation and Drainage Systems* **2011**, *25*, 215–236.

(39) Multsch, S.; Elshamy, M.; Batarseh, S.; Seid, A.; Frede, H.-G.; Breuer, L. Improving irrigation efficiency will be insufficient to meet future water demand in the Nile Basin. *Journal of Hydrology: Regional Studies* **2017**, *12*, 315–330.

(40) Osama, S.; Elkholy, M.; Kansoh, R. M. Optimization of the cropping pattern in Egypt. *Alexandria Engineering Journal* **2017**, *56*, 557–566.

(41) Muala, E.; Mohamed, Y. A.; Duan, Z.; Van der Zaag, P. Estimation of Reservoir Discharges from Lake Nasser and Roseires Reservoir in the Nile Basin Using Satellite Altimetry and Imagery Data. *Remote Sensing* **2014**, *6*, 7522–7545.

(42) Bazza, M.; Kay, M.; Knutson, C. Drought characteristics and management in North Africa and the Near East. *FAO Water Reports* **2018**,

(43) Birkett, C.; Reynolds, C.; Beckley, B.; Doorn, B. In *Coastal Altimetry*; Vignudelli, S., Kostianoy, A. G., Cipollini, P., Benveniste, J., Eds.; Springer Berlin Heidelberg: Berlin, Heidelberg, 2011; pp 19–50.

(44) Zaroug, M. A. H.; Eltahir, E. A. B.; Giorgi, F. Droughts and floods over the upper catchment of the Blue Nile and their connections to the timing of El Niño and La Niña events. *Hydrology and Earth System Sciences* **2014**, *18*, 1239–1249.

(45) Siam, M. S.; Eltahir, E. A. B. Climate change enhances interannual variability of the Nile river flow. *Nature Climate Change* **2017**, *7*, 6.

(46) Conway, D. Future Nile river flows. *Nature Climate Change* **2017**, *7*, 319–320.

(47) Zhang, Z.; Zimmermann, N. E.; Calle, L.; Hurtt, G.; Chatterjee, A.; Poulter, B. Enhanced response of global wetland methane emissions to the 2015-2016 El Niño-Southern Oscillation event. *Environmental Research Letters* **2018**, *13*, 074009, Publisher: IOP Publishing.

(48) Bastviken, D.; Cole, J.; Pace, M.; Tranvik, L. Methane emissions from lakes: Dependence of lake characteristics, two regional assessments, and a global estimate. *Global Biogeochemical Cycles* **2004**, *18*, _eprint: https://agupubs.onlinelibrary.wiley.com/doi/pdf/10.1029/2004GB002238.

(49) Wilkinson, J.; Maeck, A.; Alshboul, Z.; Lorke, A. Continuous Seasonal River Ebullition Measurements Linked to Sediment Methane Formation. *Environmental Science & Technology* **2015**, *49*, 13121–13129.

(50) Holgerson, M. A.; Raymond, P. A. Large contribution to inland water CO_2 and CH_4 emissions from very small ponds. *Nature Geoscience* **2016**, *9*, 222–226, Number: 3 Publisher: Nature Publishing Group.

(51) Aguilera, E.; Vila-Traver, J.; Deemer, B. R.; Infante-Amate, J.; Guzmán, G. I.; González de Molina, M. Methane Emissions from Artificial Waterbodies Dominate the Carbon Footprint of Irrigation: A Study of Transitions in the Food-Energy-Water-Climate Nexus (Spain, 1900-2014). *Environmental Science & Technology* **2019**, *53*, 5091–5101, Publisher: American Chemical Society.

(52) Prairie, Y. T.; Alm, J.; Beaulieu, J.; Barros, N.; Battin, T.; Cole, J.; del Giorgio, P.; Del-Sontro, T.; Guérin, F.; Harby, A.; Harrison, J.; Mercier-Blais, S.; Serça, D.; Sobek, S.; Vachon, D. Greenhouse Gas Emissions from Freshwater Reservoirs: What Does the Atmosphere See? *Ecosystems* **2018**, *21*, 1058–1071.

(53) Abril, G.; Guerin, F.; Richard, S.; Delmas, R.; GalyLacaux, C.; Gosse, P.; Tremblay, A.; Varfalvy, L.; Santos, M. A. D.; Matvienko, B. Carbon dioxide and methane emissions and the carbon budget of a 10-year old tropical reservoir (Petit Saut, French Guiana). *Global Biogeochemical Cycles* **2005**, *19*, _eprint: https://agupubs.onlinelibrary.wiley.com/doi/pdf/10.1029/2005GB002457.

(54) Kemenes, A.; Forsberg, B. R.; Melack, J. M. Methane release below a tropical hydroelectric dam. *Geophysical Research Letters* **2007**, *34*, _eprint: https://agupubs.onlinelibrary.wiley.com/doi/pdf/10.1029/2007GL029479.

(55) Artuso, F.; Chamard, P.; Piacentino, S.; di Sarra, A.; Meloni, D.; Monteleone, F.; Sferlazzo, D. M.; Thiery, F. Atmospheric methane in the Mediterranean: Analysis of measurements at the island of Lampedusa during 1995-2005. *Atmospheric Environment* **2007**, *41*, 3877–3888.

(56) Dlugokencky, E.; Lang, P.; Crotwell, A.; Mund, J.; Crotwell, M.; Thoning, K. Atmospheric Methane Dry Air Mole Fractions from the NOAA ESRL Carbon Cycle Cooperative Global Air Sampling Network, 1983-2016, Version: 2017-07-28. 2017;

ftp://aftp.cmdl.noaa.gov/data/trace_gases/ch4/flask/surface/, (accessed 19 January 2021).

Graphical TOC Entry

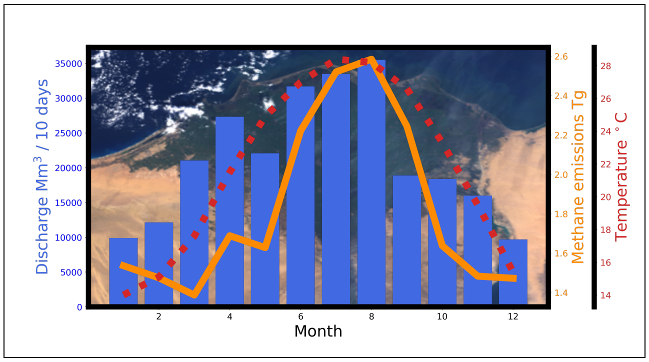

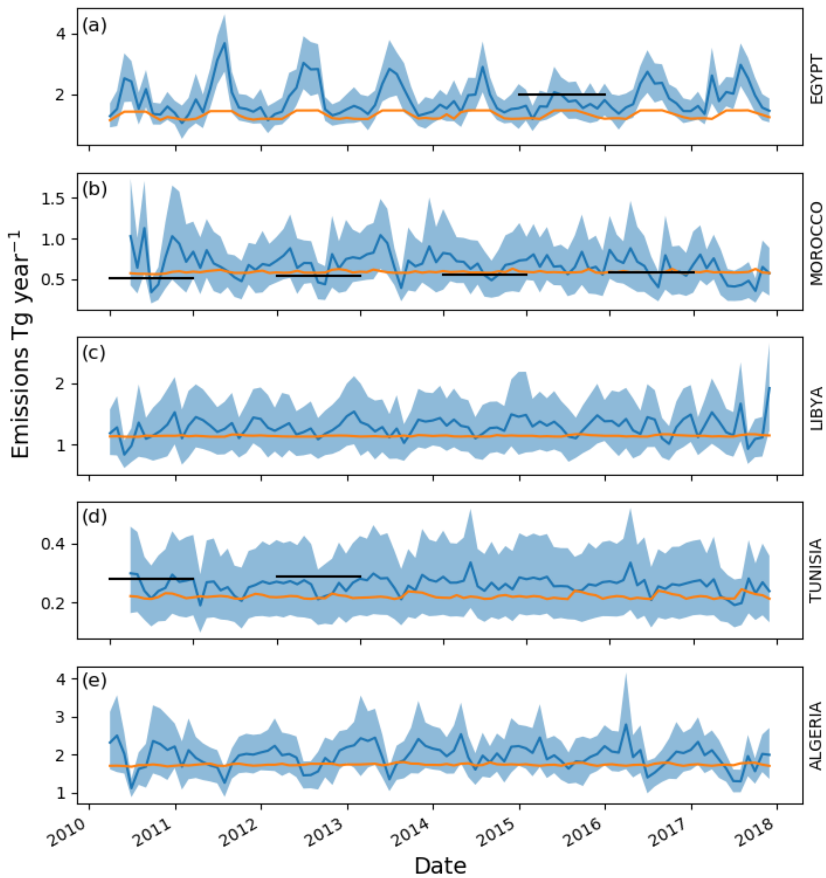

Figure 1: Emissions from countries in North Africa between 2010-2017: (a) Egypt, (b) Morocco, (c)Libya, (d) Tunisia and (e) Algeria. The blue line shows the posterior mean emissions for each month, and the blue shading shows the 95 % HPD region. The orange line shows the a priori emissions for each country, and the black lines show annual emissions reported to the UNFCCC.

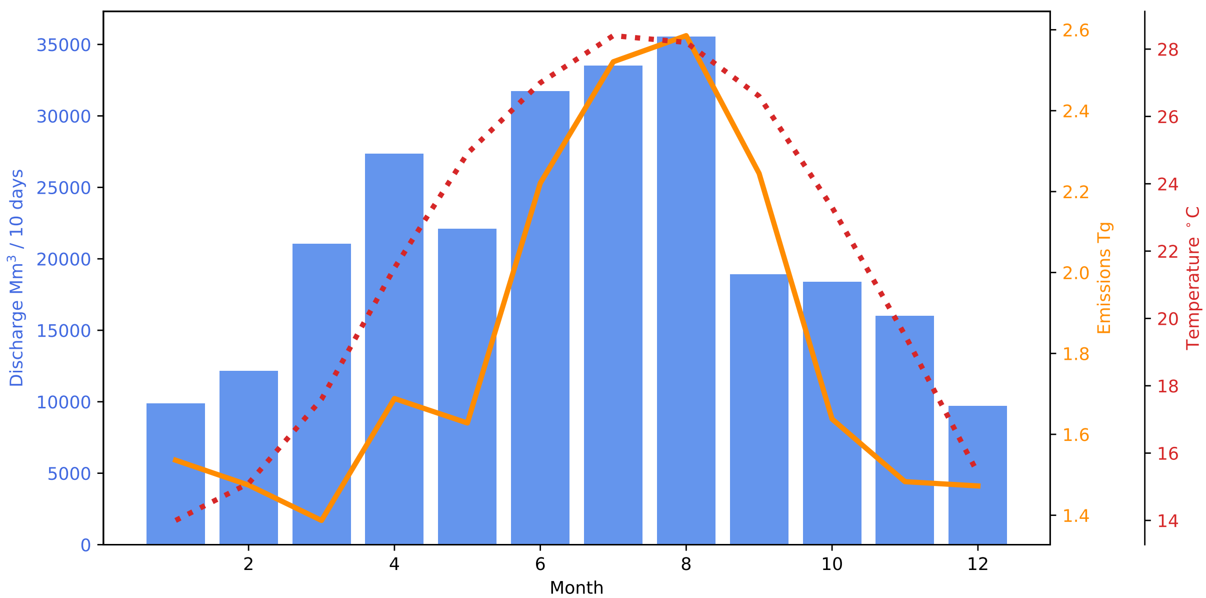

Figure 2: The mean posterior estimated emissions for Egypt for each month between 2010-2017 (orange), the daily mean temperature at Cairo for each month (red), and the monthly satellite-estimated discharge from Lake Nasser (feeding the Nile after the Aswan High Dam) from 2005-2008[41] (blue).

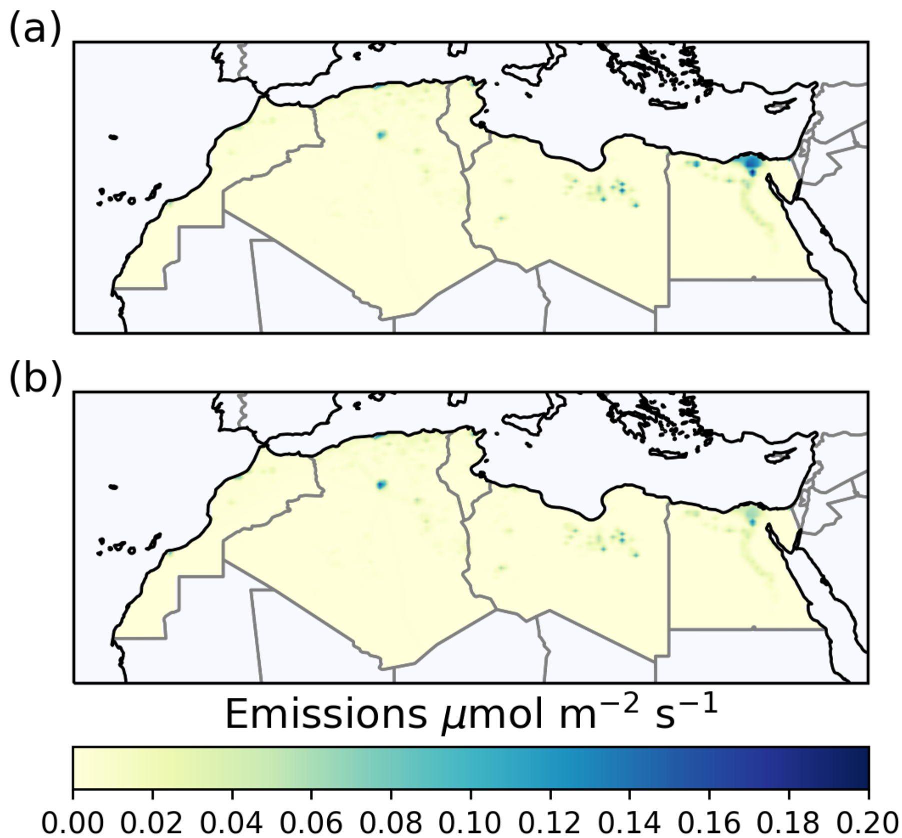

Figure 3: A map showing (a) the posterior mean estimated flux and (b) the a priori flux from the North African region as an average for August over all years.

Supplement to: Estimates of North African methane emissions from 2010-2017 using GOSAT observations

Luke M. Western,*,† Alice E. Ramsden,‡ Anita L. Ganesan,‡ Hartmut Boesch,¶,§ Robert J. Parker,¶,§ Tia R. Scarpelli,‖ Rachel L. Tunnicliffe,† and Matthew Rigby†

†*School of Chemistry, University of Bristol, Bristol, BS8 1TS, UK*

‡*School of Geographical Sciences, University of Bristol, Bristol, BS8 1SS, UK*

¶*National Centre for Earth Observation, University of Leicester, Leicester, LE1 7RH, UK*

§*Earth Observation Science, School of Physics and Astronomy, University of Leicester, Leicester, LE1 7RH, UK*

‖*Earth and Planetary Sciences, Harvard University, Cambridge, 02138, USA*

E-mail: luke.western@bristol.ac.uk

North African petroleum and natural gas production

Production of petroleum products in Algeria, the main producer in the region, have remained steady over the period of study, at around 1881 thousand barrels per day (TBPD) in 2010, reducing to around 1637 TBPD by the end of 2017[1] (Figure S1). Libya, the second largest producer, has had large fluctuations in production since the Arab Spring[2], starting in Febrary 2011. Production has not recovered since 2010, where annual production was 1844 TBPD, and hit an annual low of 478 TBPD in 2016. Production in Egypt has remained fairly constant over the period of study, with annual production varying between 655 - 714 TBPD. Natural gas production is again largest in Algeria, followed by Egypt. Production in Algeria remained largely unchanged between 2010-2015 (∼185 billion cubic metres, BCM), and declined slightly in Egypt from 67 to 49 BCM between 2010-2015. Libya's post-2010 gas production is much smaller in comparison (10-18 BCM), but was 30 BCM in 2010. Tunisia and Morocco are comparatively minor producers of oil and gas.

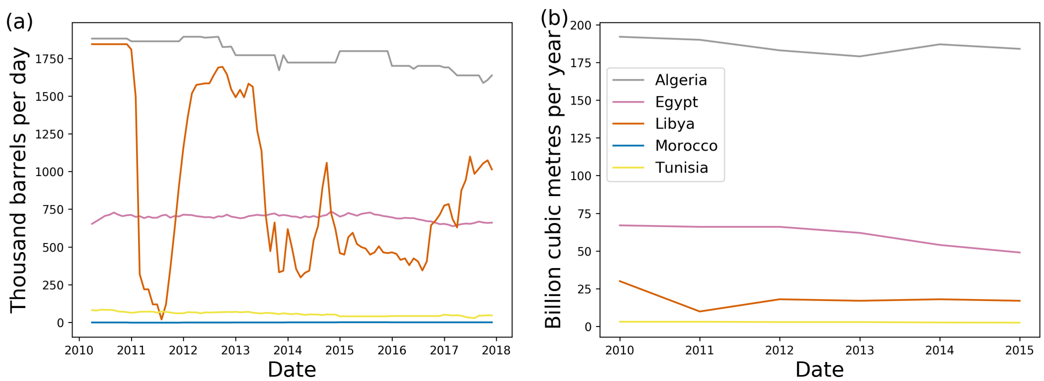

Figure S1: Oil (a) and natural gas (b) production in Algeria, Egypt, Libya, Morocco and Tunisia. Any natural gas production in Morocco was negligible. Production data for natural gas were only available until 2015. The data are from the U.S. Energy Information Administration[1].

Results using different a priori boundary conditions

We repeat our results to test the influence of the chosen a priori mole fraction at the model domain boundary. The inverse method and sensitivity to the boundaries was treated as in the main text, but with the a priori mole fraction at the domain boundary taken from the ECMWF CAMS CH_4 flux inversion product v17r1 (`https://ads.atmosphere.copernicus.eu/cdsapp#!/dataset/cams-global-greenhouse-gas-inversion?tab=overview`, accessed 22 April 2021). The data product is produced using surface observations only. See `https://atmosphere.copernicus.eu/sites/default/files/2018-12/CAMS73_2015SC3_D73.2.4.4-2017_201811_validation_1990-2017_v1.pdf` for more information (accessed 22 April

2021).

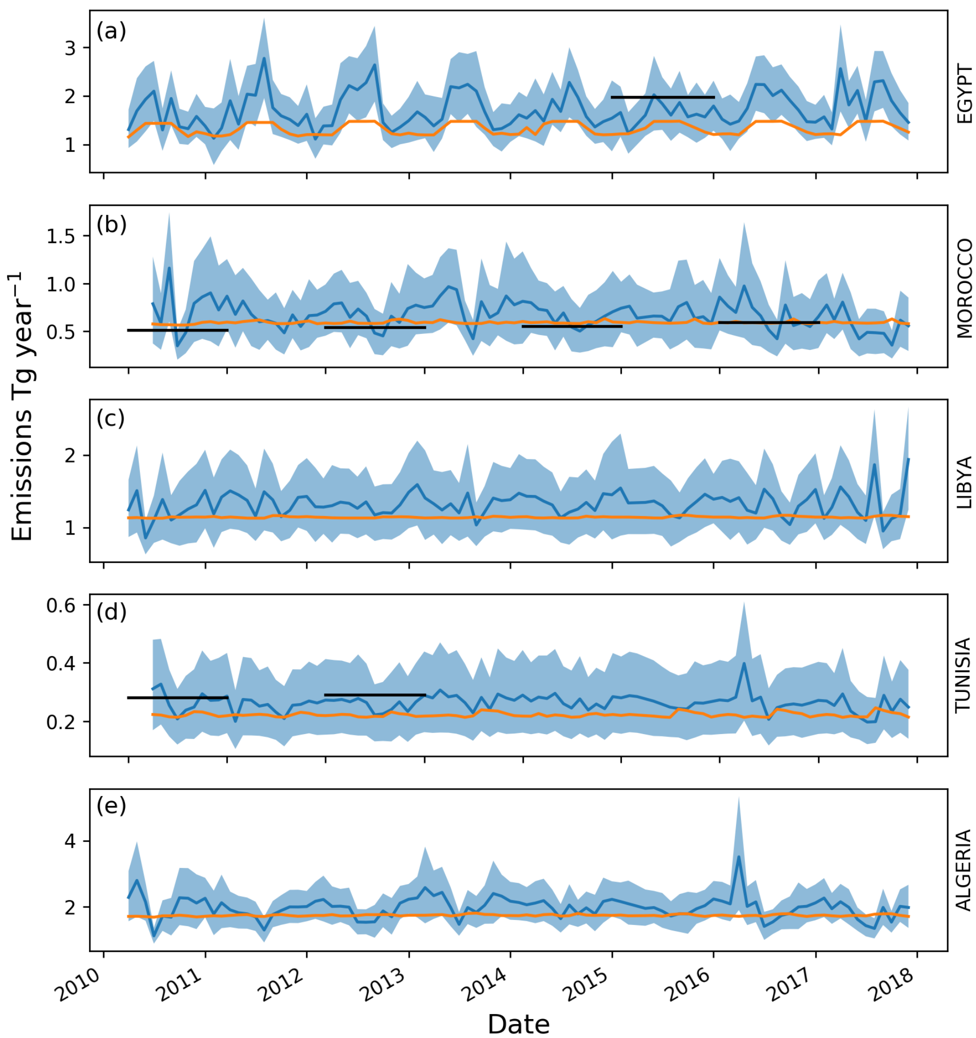

Figure S2: Emissions from countries in North Africa between 2010-2017 using different a priori mole fractions at the boundary to that in the main text. (a) Egypt, (b) Morocco, (c) Libya, (d) Tunisia and (e) Algeria. The blue line shows the posterior mean emissions for each month, and the blue shading shows the 95 % HPD region. The orange line shows the a priori emissions for each country, and the black lines show annual emissions reported to the UNFCCC.

Figure S2 shows the emissions time series from the five North African countries (as Figure 1, main text) using the alternate a priori mole fraction at the boundary, as described. Emissions do not change substantially from those presented in the main text and do not change any of the conclusions drawn, although some small differences exist. Most notably, summertime emissions peaks in Egypt are not as high as in the main text, but still remain elevated above that observed in the a priori emissions estimates and exhibit a seasonal cycle.

Highest Posterior Density region

The Highest Posterior Density (HPD) region is the narrowest region, R, in the total posterior parameter space that holds probability content $(1-\alpha)$. This is achieved if the following conditions are fulfilled,

1. $\mathrm{p}\{\mathbf{x} \in R \mid \mathbf{y}\} = (1-\alpha)$
2. for $\mathbf{x}_1 \in R$ and $\mathbf{x}_2 \notin R$, $\mathrm{p}(\mathbf{x}_1 \mid \mathbf{y}) \geq \mathrm{p}(\mathbf{x}_2 \mid \mathbf{y})$.

Agricultural emissions outside of Egypt

Unlike in Egypt, where irrigation for agriculture is dependent on the Nile, agricultural practices in the rest of North Africa are dependent on precipitation as their main water source[3]. The agricultural sector is the largest contributor to gross domestic product in both Algeria and Libya[3]. There is more rainfall in North Africa during the Northern Hemisphere winter, when temperatures are lower, with little rainfall and high temperatures during the Northern Hemisphere summer[4–6]. Therefore, it is expected, given the observations in Egypt, that emissions from agronomically managed temporary wetlands in North Africa, other than Egypt, would have higher emissions in winter months (during their crop growing season with maximum rainfall), than in the summer months. In addition, livestock in North Africa are slaughtered during times of fodder scarcity, leading to lower emissions from ruminants during times of low rainfall[3].

A pattern of higher North African methane emissions in winter months during the agricultural season is somewhat apparent in our inferred emissions (see Figure 1, main text), particularly in Algeria, although to a much lesser extent than the seasonality in Egypt. This may be explained by the lower temperatures during the agricultural season, in contrast to high summer temperatures during Egypt's agricultural season, leading to lower rates of methanogenesis[7–10].

Validation against measurements made at Lampedusa

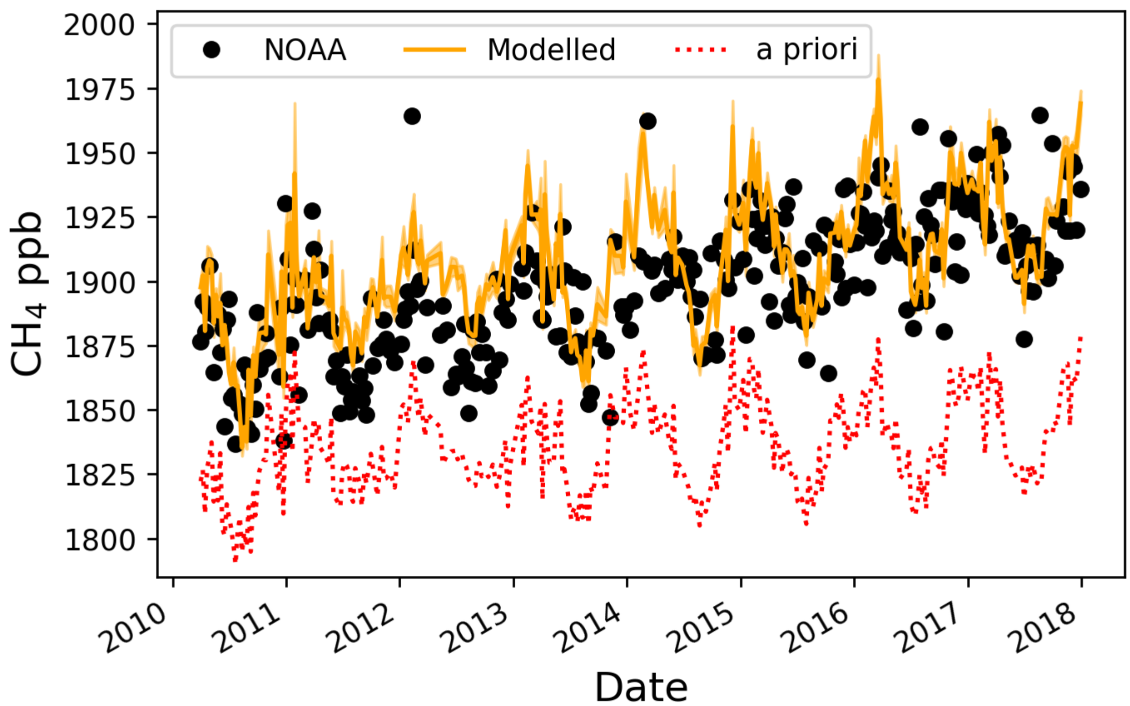

Figure S3: Methane concentrations (black circles) measured at Lampedusa measurement station (12.62°E, 35.52°N) and forward modelled concentrations (orange lines) using the estimated emissions and NAME-derived sensitivities. Also shown are the forward modelled a priori concentrations (dotted red line), modelled using the a priori emissions and NAME-derived sensitivities.

The paucity of in situ measurement data in the region of study, which motivates the use satellite-observation derived emissions, makes detailed validation against an independent dataset difficult. Here we validate our emissions by comparing our posterior model to weekly flask-air samples from the Italian island of Lampedusa[11,12] (12.62°E, 35.52°N).

The modelled concentrations are calculated from NAME footprints, simulated using

20,000 particles released for a 1-hour period when each measurement was made at a height of 10 ± 10 metres above ground level. The particles were tracked for 30 days and their interaction with the surface and boundaries were recorded as described for GOSAT in the main text.

Given the low frequency of the measurements, which are made to sample background conditions, a rigorous validation of the posterior emissions is difficult. In addition, errors in the transport and meteorology using NAME may compound errors in the forward modelled concentrations using GOSAT- and NAME-derived emissions estimates. It is clear, however, that the posterior mean predicted mole fractions greatly improve the fit to observations over the a priori predicted concentrations, as can be seen in Figure , where the a priori predicted concentration falls far below the observations. Some simple statistics using the posterior mean predicted and a priori predicted mole fraction shows an improvement to the root-mean-square error from 66 ppb to 21 ppb, and an improvement to the R^2 statistic from 0.37 to 0.54.

Supplementary Tables and Figures

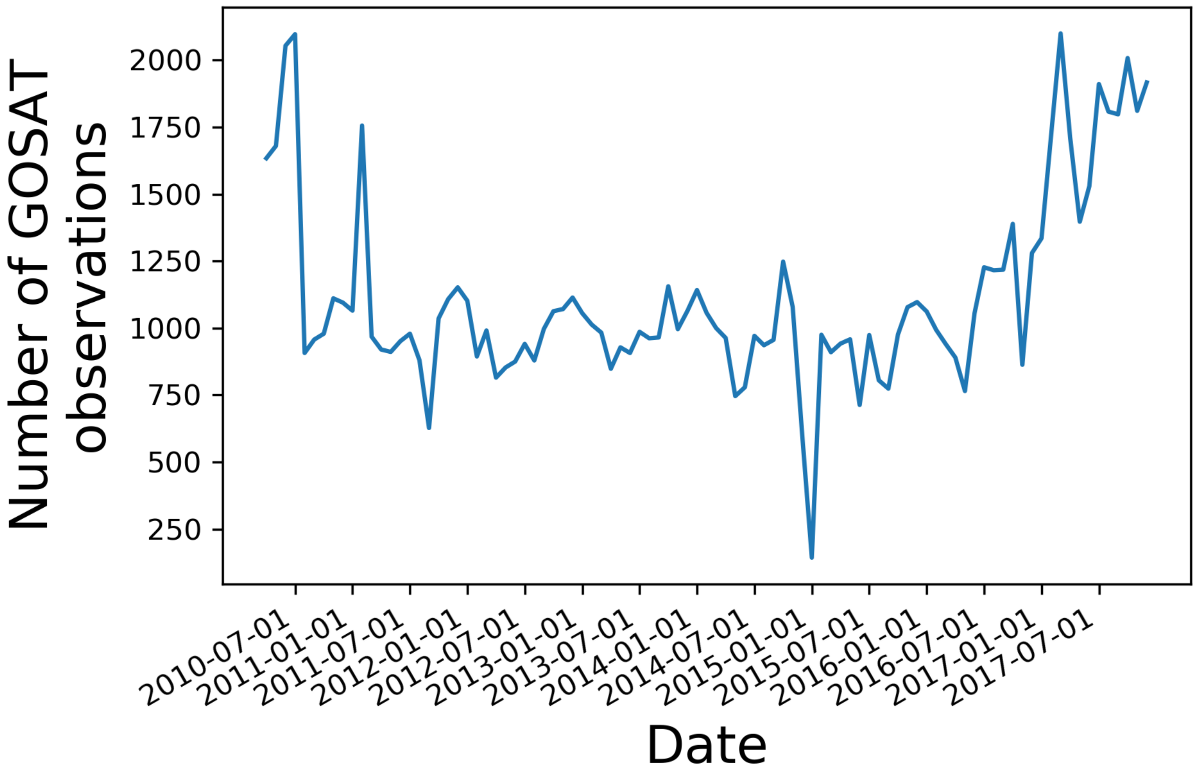

Figure S4: The number of GOSAT $XCH_{4\,\mathrm{proxy}}$ observations per month used in the inversion.

Table S1: Annual estimates of mean posterior methane emissions and the 95% uncertainty range. The annual emissions are estimated from the monthly estimates within each year, assuming that the posterior distributions are independent, which will most likely underestimate the true annual uncertainty.

	Annual emissions (Tg year^{-1})				
Year	Egypt	Morocco	Libya	Tunisia	Algeria
2010	1.50 (1.35, 1.66)	0.78 (0.62, 0.94)	1.16 (1.01, 1.30)	0.27 (0.22, 0.31)	2.00 (1.75, 2.25)
2011	1.76 (1.60 1.93)	0.65 (0.56, 0.74)	1.31 (1.18, 1.45)	0.24 (0.21, 0.28)	1.80 (1.65, 1.96)
2012	1.64 (1.49, 1.80)	0.67 (0.58, 0.77)	1.26 (1.13, 1.39)	0.25 (0.22, 0.29)	1.85 (1.71, 2.00)
2013	1.64 (1.48, 1.79)	0.75 (0.64, 0.86)	1.31 (1.17, 1.45)	0.26 (0.22, 0.30)	2.07 (1.88, 2.26)
2014	1.61 (1.47, 1.75)	0.66 (0.57, 0.77)	1.32 (1.19, 1.45)	0.27 (0.23, 0.31)	2.01 (1.84, 2.18)
2015	1.49 (1.34, 1.64)	0.69 (0.59, 0.79)	1.33 (1.19, 1.47)	0.27 (0.23, 0.30)	2.00 (1.83, 2.17)
2016	1.77 (1.63, 1.92)	0.65 (0.55, 0.75)	1.30 (1.17, 1.43)	0.26 (0.22, 0.29)	1.95 (1.77, 2.14)
2017	1.82 (1.67, 1.98)	0.55 (0.48, 0.63)	1.33 (1.20, 1.46)	0.23 (0.20, 0.27)	1.82 (1.68, 1.96)

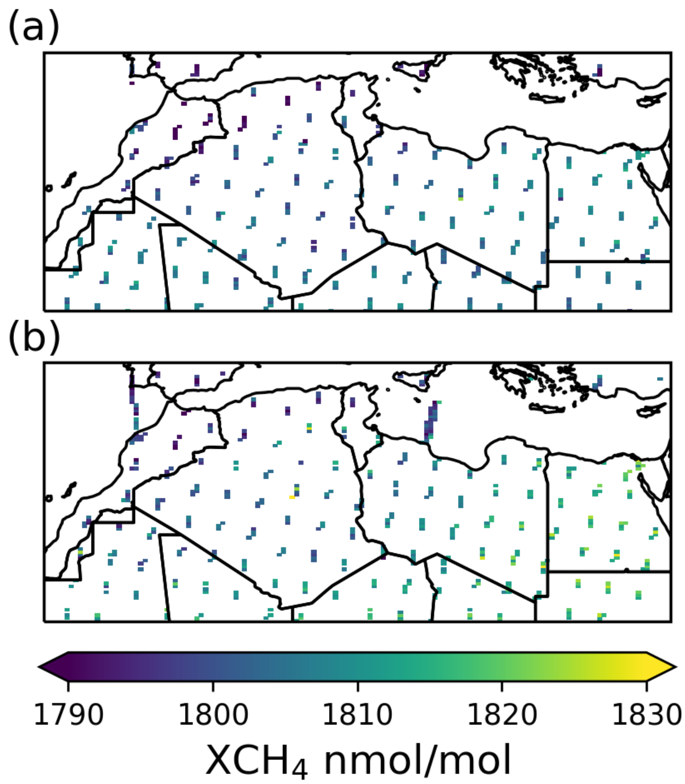

Figure S5: The average GOSAT $XCH_{4\,proxy}$ observations binned to the resolution of the NAME dispersion model output for (a) November 2011 - April 2012 and (b) May 2012 - October 2012.

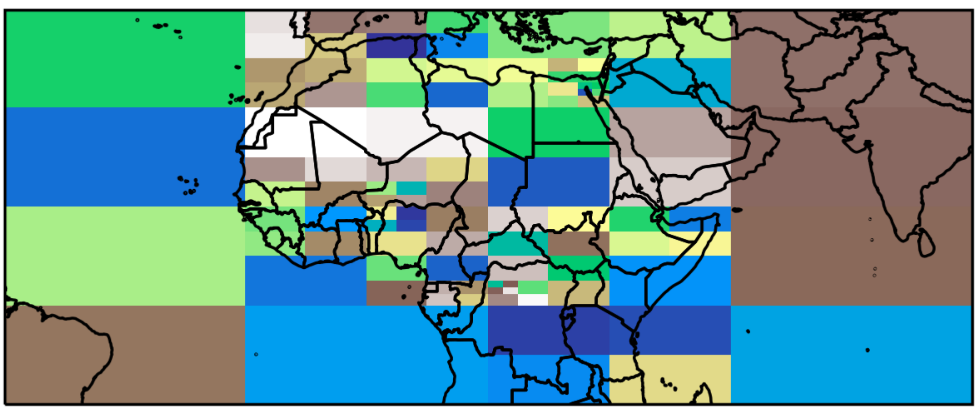

Figure S6: The basis functions representation of the emissions within the model domain for March 2013.

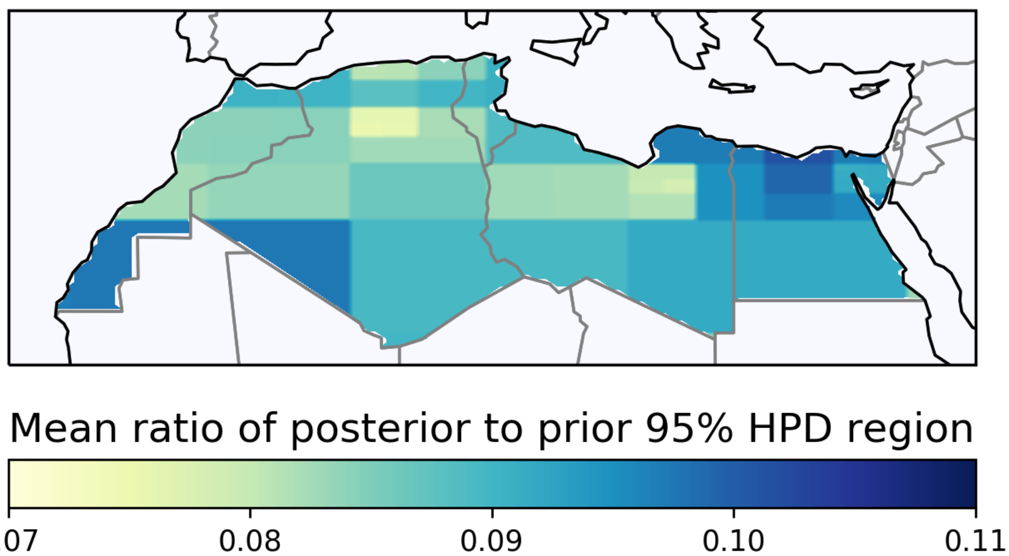

Figure S7: The mean ratio of the range of the upper and lower bounds of the posterior to prior 95% HPD region in space. This mean is over all months estimated within the study. The map shows that, on average in the region of study, the range between the 97.5% and 2.5% uncertainty bound in the posterior distribution is, at most, 10% of that in the prior, or, equivalently, shows at least a 90% uncertainty reduction.

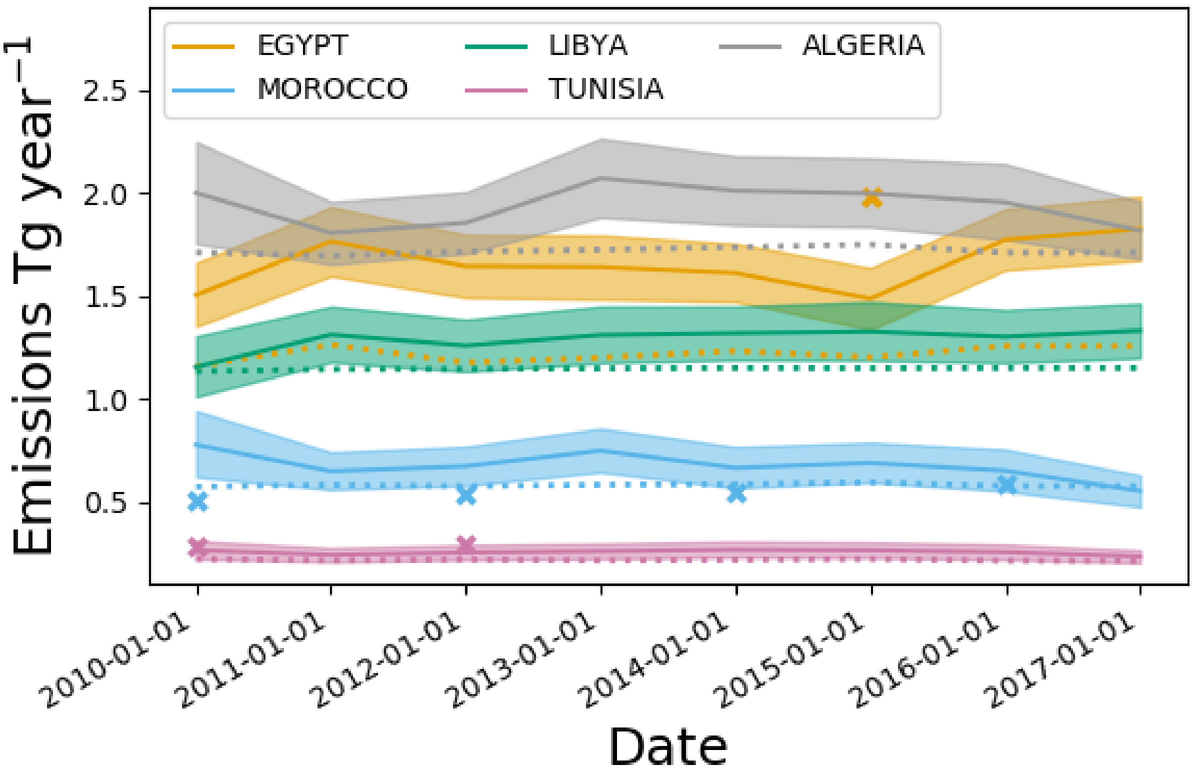

Figure S8: Methane emissions estimates in North Africa presented as annual means. The lines are posterior mean emissions estimates, and the shading shows the 95% posterior uncertainty. The dashed line shows the annual mean a priori emissions estimate and the crosses show estimates of methane emissions submitted as national reporting to the UNFCCC. The emissions estimates are tabulated in Table S1. The annual emissions are estimated from the monthly estimates within each year, assuming that the posterior distributions are independent, which will most likely underestimate the true annual uncertainty.

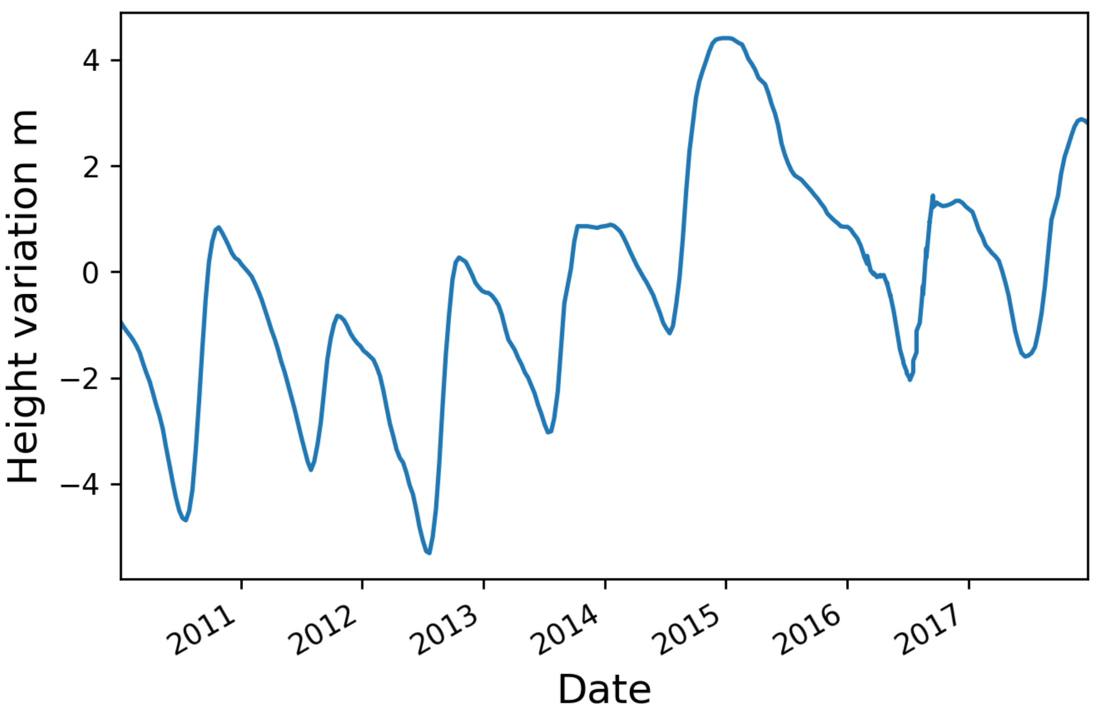

Figure S9: Lake Nasser water level from satellite radar and altimetry[13]. The water level generally drops and rises during midsummer, although 2015 seems anomalous in this trend.

References

(1) EIA, EIA: International Energy Statistics. `http://eia.gov/beta/international/` (accessed 22 January 2021).

(2) Bahgat, G. The impact of the Arab spring on the oil and gas industry in North Africa: a preliminary assessment. *The Journal of North African Studies* **2012**, *17*, 503–514.

(3) Schilling, J.; Freier, K. P.; Hertig, E.; Scheffran, J. Climate change, vulnerability and adaptation in North Africa with focus on Morocco. *Agriculture, Ecosystems & Environment* **2012**, *156*, 12–26.

(4) Chourghal, N.; Lhomme, J. P.; Huard, F.; Aidaoui, A. Climate change in Algeria and its impact on durum wheat. *Regional Environmental Change* **2016**, *16*, 1623–1634.

(5) Salhi, A.; Martin-Vide, J.; Benhamrouche, A.; Benabdelouahab, S.; Himi, M.; Benabdelouahab, T.; Casas Ponsati, A. Rainfall distribution and trends of the daily precipitation concentration index in northern Morocco: a need for an adaptive environmental policy. *SN Applied Sciences* **2019**, *1*, 277.

(6) Aieb, A.; Lefsih, K.; Scarpa, M.; Bonaccorso, B.; Cicero, N.; Mimeche, O.; Madani, K. Statistical modeling of monthly rainfall variability in Soummam watershed of Algeria, between 1967 and 2018. *Natural Resource Modeling* **2020**, *33*, e12288, _eprint: https://onlinelibrary.wiley.com/doi/pdf/10.1111/nrm.12288.

(7) Bastviken, D.; Cole, J.; Pace, M.; Tranvik, L. Methane emissions from lakes: Dependence of lake characteristics, two regional assessments, and a global estimate. *Global Biogeochemical Cycles* **2004**, *18*, _eprint: https://agupubs.onlinelibrary.wiley.com/doi/pdf/10.1029/2004GB002238.

(8) Wilkinson, J.; Maeck, A.; Alshboul, Z.; Lorke, A. Continuous Seasonal River Ebulli-

tion Measurements Linked to Sediment Methane Formation. *Environmental Science & Technology* **2015**, *49*, 13121–13129.

(9) Holgerson, M. A.; Raymond, P. A. Large contribution to inland water CO_2 and CH_4 emissions from very small ponds. *Nature Geoscience* **2016**, *9*, 222–226, Number: 3 Publisher: Nature Publishing Group.

(10) Aguilera, E.; Vila-Traver, J.; Deemer, B. R.; Infante-Amate, J.; Guzmán, G. I.; González de Molina, M. Methane Emissions from Artificial Waterbodies Dominate the Carbon Footprint of Irrigation: A Study of Transitions in the Food-Energy-Water-Climate Nexus (Spain, 1900-2014). *Environmental Science & Technology* **2019**, *53*, 5091–5101, Publisher: American Chemical Society.

(11) Artuso, F.; Chamard, P.; Piacentino, S.; di Sarra, A.; Meloni, D.; Monteleone, F.; Sferlazzo, D. M.; Thiery, F. Atmospheric methane in the Mediterranean: Analysis of measurements at the island of Lampedusa during 1995-2005. *Atmospheric Environment* **2007**, *41*, 3877–3888.

(12) Dlugokencky, E.; Lang, P.; Crotwell, A.; Mund, J.; Crotwell, M.; Thoning, K. Atmospheric Methane Dry Air Mole Fractions from the NOAA ESRL Carbon Cycle Cooperative Global Air Sampling Network, 1983-2016, Version: 2017-07-28. 2017; `ftp://aftp.cmdl.noaa.gov/data/trace_gases/ch4/flask/surface/`, (accessed 19 January 2021).

(13) Birkett, C.; Reynolds, C.; Beckley, B.; Doorn, B. In *Coastal Altimetry*; Vignudelli, S., Kostianoy, A. G., Cipollini, P., Benveniste, J., Eds.; Springer Berlin Heidelberg: Berlin, Heidelberg, 2011; pp 19–50.